In Vivo 3D MRI Staining of Mouse Brain After Subcutaneous Application of $MnCl_2$

Takashi Watanabe, Oliver Natt, Susann Boretius, Jens Frahm, and Thomas Michaelis*

Follow-up T_1-weighted 3D gradient-echo MRI (2.35 T) of murine brain in vivo ($N = 5$) at 120 μm isotropic resolution revealed spatially distinct signal increases 6–48 hr after subcutaneous application of $MnCl_2$ (20 mg/kg). The effects result from a shortening of the water proton T_1 relaxation time due to the presence of unchelated paramagnetic Mn^{2+} ions, which access the brain by systemic circulation and crossing of the blood–brain barrier (BBB). A pronounced Mn^{2+}-induced signal enhancement was first seen in structures without a BBB, such as the choroid plexus, pituitary gland, and pineal gland. Within 24 hr after administration, Mn^{2+} contrast highlighted the olfactory bulb, inferior colliculi, cerebellum, and the CA3 subfield of the hippocampus. The affinity of Mn^{2+} to various brain systems suggests the neuronal uptake of Mn^{2+} ions from the extracellular space and subsequent axonal transport. Thus, at least part of the Mn^{2+} contrast reflects a functional brain response of behaving animals, for example, in the olfactory system. In vivo MRI staining of the brain by systemic administration of $MnCl_2$ may contribute to phenotyping mutant mice with morphologic and functional alterations of the central nervous system. Magn Reson Med 48:852–859, 2002. © 2002 Wiley-Liss, Inc.

Key words: magnetic resonance imaging; mouse; brain; manganese; hippocampus

Progress in neurogenetics has renewed interest in imaging neuroscience because 1) it can improve our understanding of the structure and function of the central nervous system in the context of genetic information, and 2) it can be used to evaluate novel therapeutic interventions in active animals. In either case, gene technology has led to the use of an increasing number of mutant mice, which requires the use of in vivo assessments such as, for example, those offered by noninvasive MRI techniques. Several in vivo MRI studies of mouse brain have demonstrated potential for providing detailed morphologic insights (1–6). Nevertheless, the anatomic information obtainable is limited and a considerable number of abnormalities may still have to be verified by other methods because of their microscopic size, sparse distribution, and/or poor MRI detectability caused by subtle alterations of MR properties. Therefore, additional means of achieving soft-tissue contrast enhancement or MRI staining (7) by exogenous compounds are highly desirable.

Because common MRI contrast agents consist of chelated paramagnetic ions, their systemic application does not lead to a penetration of the blood-brain barrier (BBB). Such contrast agents are safe for human studies and can be used clinically to detect disturbances of the BBB. The situation differs for free divalent metal ions, which exhibit variable degrees of neurotoxicity. In particular, high-resolution autoradiography has demonstrated that manganese accumulates in the olfactory bulb, olfactory nuclei, inferior colliculi, amygdala, thalamus, hippocampal formation, and cerebellum (8–12). Upon bolus injection, Mn^{2+} enters the brain across the capillary endothelium (13–15) and leads to biologic halflives of 51–74 days (9). In conjunction with its well-known capabilities as a paramagnetic MRI contrast agent that effectively reduces the T_1 relaxation time of accessible water protons (16), these data suggest that Mn^{2+} is a good candidate for MRI staining of animal brain after systemic administration.

Previous MRI studies of manganese in animal brain addressed its regional distribution and cerebral toxicity during an acute phase 3–22 hr after Mn^{2+} exposure in rat brain (17) or in response to chronic poisoning (of several months duration) in rabbits and monkeys (18,19). In contrast to the autoradiography results, however, the MRI studies failed to report any signal enhancement in structures such as the olfactory bulb or hippocampal formation. Most likely, however, this observation can be ascribed to the limited spatial resolution available and the concomitant elimination of anatomic contrast by significant partial volume effects of small (but distinct) neighboring structures. The purpose of this work was to combine the development of a high-resolution T_1-weighted 3D MRI approach to mouse brain in vivo with the subcutaneous application of $MnCl_2$. The primary aim was to achieve a more sensitive access to Mn^{2+}-induced soft-tissue contrast and thereby improve the delineation of specific cerebral microstructures.

MATERIALS AND METHODS

Animals and Anesthesia

Animal studies were performed in accordance with German animal protection laws after approval was given by the responsible governmental authority. Female NMRI mice (4–6 weeks old, 24–28 g, $N = 5$) received a 0.4% $MnCl_2$ solution (20 mg/kg) within a glucose solution (4.2%) via subcutaneous injections into the axillary adipose tissue of both sides. Animals were fasted for 8 hr prior to MRI examinations.

Anesthesia was induced by i.p. injection of xylazine (12.5 mg/kg), ketamine (125 mg/kg), and atropine (0.08 mg/kg). The animals were intubated with a purpose-built polyethylene endotracheal tube (0.58 mm inner diameter, 0.96 mm outer diameter) and artificially ventilated using an animal respirator (Rhema, Germany) with an inspiratory time of 0.1 s, a respiratory rate of 120 breaths per minute, and an estimated tidal volume of 0.15–0.25 ml. Anesthesia was

Biomedizinische NMR Forschungs GmbH am Max-Planck-Institut für biophysikalische Chemie, Göttingen, Germany.

*Correspondence to: T. Michaelis, Ph.D., Biomedizinische NMR Forschungs GmbH, 37070 Göttingen, Germany. E-mail: tmichae@gwdg.de

Received 26 March 2002; revised 12 June 2002; accepted 16 July 2002.

DOI 10.1002/mrm.10276

Published online in Wiley InterScience (www.interscience.wiley.com).

Table 1
SNR of Enhanced Structures in Murine Brain After Subcutaneous $MnCl_2$

Region	ROI (mm^2)	Basal (N = 3)	6 hr (N = 3)	24 hr (N = 4)	48 hr (N = 4)
Choroid plexus	0.25	28.7 ± 0.8	63.3 ± 1.3[a]	43.1 ± 6.6[a]	35.5 ± 1.5[a]
Pineal gland	0.10	32.3 ± 5.7	57.6 ± 1.0[a]	36.2 ± 2.5	33.1 ± 1.6
Posterior pituitary	0.13	50.5 ± 2.7	59.3 ± 3.7[a]	53.0 ± 2.3	54.0 ± 1.3
Anterior pituitary	0.20	37.3 ± 2.1	56.3 ± 7.0[a]	55.1 ± 5.5[a]	58.7 ± 5.9[a]
Frontal cortex	0.26	34.7 ± 0.5	36.2 ± 1.8	35.3 ± 2.9	35.8 ± 2.2
Basal ganglia	0.40	31.1 ± 0.3	33.8 ± 2.2	32.5 ± 3.0	33.5 ± 1.8
Olfactory bulb	2.10	34.5 ± 0.6	39.1 ± 2.2	42.8 ± 4.3[a]	41.5 ± 2.7[a]
Anterior forebrain	0.10	29.5 ± 0.6	31.3 ± 2.1	36.1 ± 3.4[a]	37.0 ± 3.0[a]
Inferior colliculus	0.70	43.7 ± 0.3	43.7 ± 2.3	45.8 ± 5.0	47.8 ± 3.2
Cerebellum	0.50	38.8 ± 0.3	41.5 ± 1.8	42.2 ± 4.5	42.9 ± 2.6[a]
Hippocampus[b]	0.53	27.4 ± 2.0	32.4 ± 4.5	29.2 ± 1.8	30.4 ± 1.0
CA3	0.15	37.1 ± 1.4	39.5 ± 2.5	40.7 ± 3.7	40.9 ± 2.3[a]
Dentate gyrus	0.10	37.2 ± 1.5	38.9 ± 2.7	41.0 ± 4.2	42.2 ± 1.3[a]

The data represent mean values ± SD averaged across animals.
[a]$P < 0.05$ (unpaired t-test vs. basal).
[b]Stratum radiatum and stratum lacunosum-moleculare of the Ammon's horn.

maintained using 0.2–0.6% halothane in a 7:3 mixture of N_2O and O_2. For MRI the animals were placed in a prone position on a purpose-built palate holder equipped with an adjustable nose cone. A heated water blanket and bed were used to maintain rectal body temperature at 37 ± 1°C. To minimize risks of complications from frequently repeated anesthesia, T_1-weighted 3D MRI data sets were acquired before Mn^{2+} administration (mice A–C) as well as 6 hr (mice A, D, and E), 24 hr (mice B–E), and 48 hr (mice A–D) after Mn^{2+} administration. After each measurement the animals were recovered from anesthesia and returned to their cages with free access to food and water.

MRI

MRI was carried out at 2.35 T using an MRBR 4.7/400-mm magnet (Magnex Scientific, Abingdon, UK) equipped with B-GA20 gradients (200 mm inner diameter, 100 mT m^{-1} maximum strength) and driven by a DBX system (Bruker Biospin, Ettlingen, Germany). Radiofrequency excitation and signal reception were accomplished with use of a Helmholtz coil (100 mm) and an elliptical surface coil (20 mm anterior–posterior, 12 mm left–right), respectively. High-resolution data sets were acquired using a T_1-weighted 3D gradient-echo MRI sequence (RF-spoiled 3D fast low-angle shot (FLASH), repetition time (TR) = 22 ms, echo time (TE) = 8.2 ms, receiver bandwidth = 17.9 kHz, flip angle = 30°) at an isotropic voxel resolution of 120 μm × 120 μm × 120 μm (field of view (FOV) = 30.72 mm × 15.36 mm × 15.36 mm in conjunction with an acquisition matrix of 256 × 106 × 106 zero-filled to 256 × 128 × 128 during image reconstruction). Signal averaging (24 accumulations) led to a measuring time of 99 min.

For quantitative evaluations, the signal-to-noise ratio (SNR) of selected brain structures, here defined as the MRI signal intensity divided by the standard deviation (SD) of the noise, was determined using software supplied by the manufacturer. Anatomic cross-sections were obtained by multiplanar reconstructions from the original 3D MRI data sets. The analysis followed a strategy previously developed for intraindividual comparisons of follow-up MRI after intraocular Mn^{2+} administration (20). Standardized regions of interest (ROIs) were selected in murine brain in close accordance with resolved anatomic structures.

RESULTS AND DISCUSSION

Subcutaneous application of $MnCl_2$ led to spatially distinct signal increases within all of the animal brains. Table 1 summarizes the SNR of multiple enhancing structures as a function of time after injection relative to basal values. As demonstrated in Fig. 1 for selected regions, the kinetic behavior leads to a gross separation of two different types

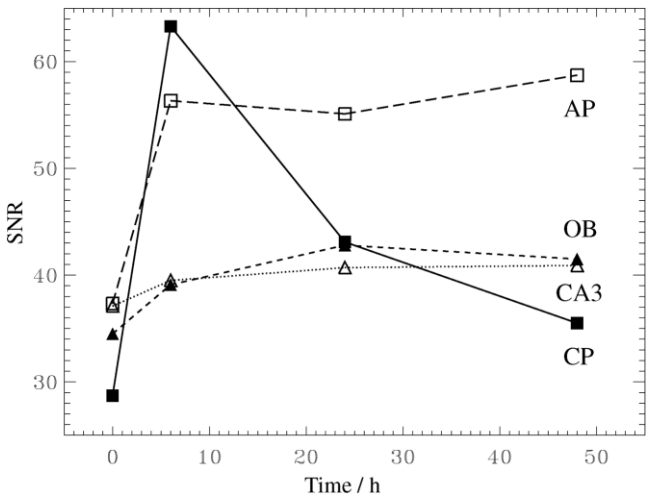

FIG. 1. Time course of mean SNR values in selected structures of murine brain before subcutaneous Mn^{2+} administration (mice A–C), and 6 hr (mice A, D, and E), 24 hr (mice B–E), and 48 hr (mice A–D) after Mn^{2+} administration. Maximum SNR increases are observed in the choroid plexus (CP) and anterior pituitary (AP) gland, which are accessible by systemic circulation. In contrast, the need to cross the BBB, and the neuronal uptake of Mn^{2+} causes a slower and weaker enhancement in brain systems such as the olfractory bulb (OB) and the CA3 region of the hippocampus.

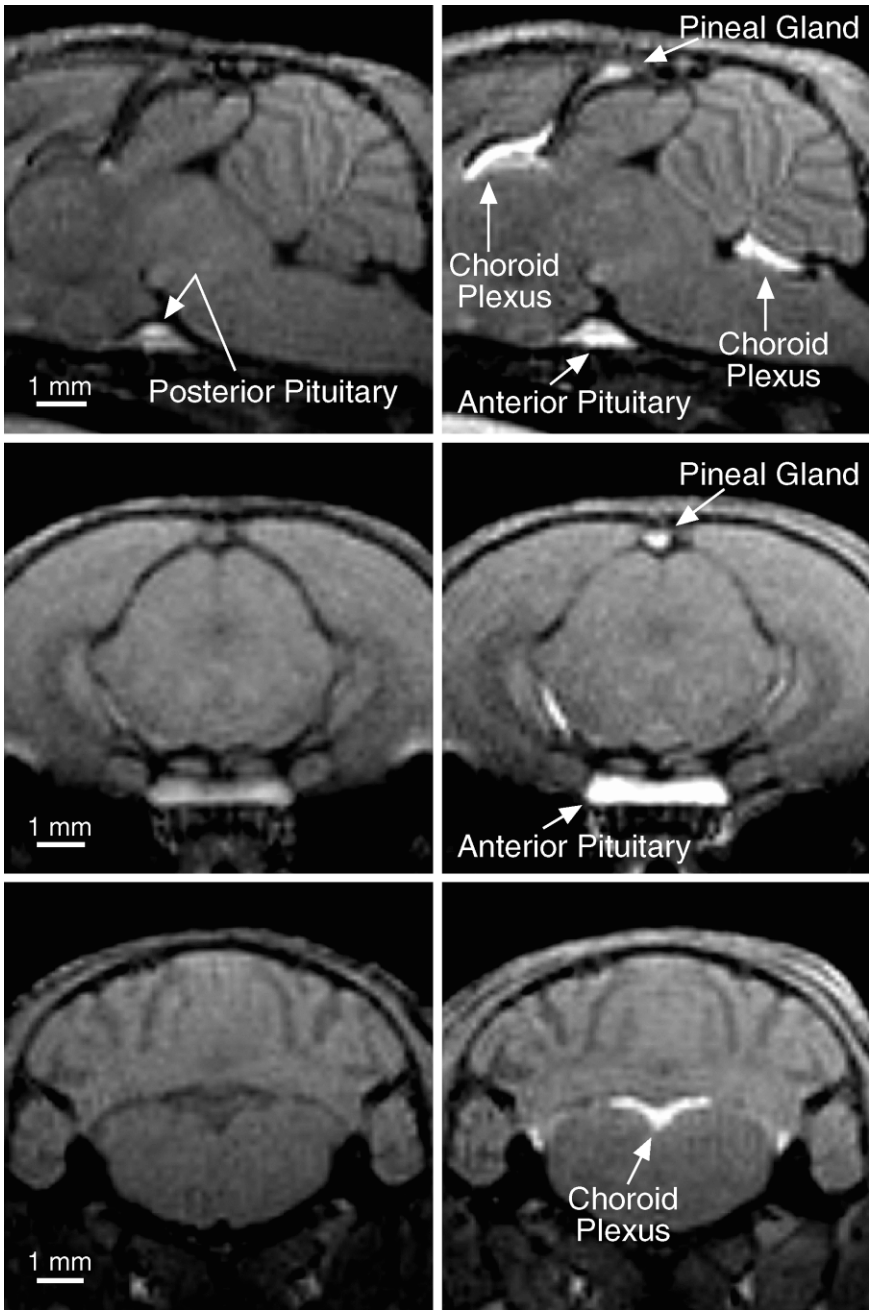

FIG. 2. T_1-weighted MRI (3D FLASH, TR/TE = 22/8 ms, flip angle = 30°, 120 μm isotropic resolution) of the brain of an anesthetized mouse (left) before and (right) 6 hr after subcutaneous $MnCl_2$ (20 mg/kg). Top: Signal enhancement in the choroid plexus and the pineal and pituitary glands in a midsagittal section. The pineal and pituitary glands (middle) and the choroid plexus (bottom) within the fourth ventricle in corresponding coronal sections.

of Mn^{2+}-induced signal enhancement. A pronounced and relatively fast enhancement, i.e., about a twofold increase in SNR after 6 hr, is seen in the choroid plexus as well as in intracranial endocrine tissue. In contrast, brain structures such as the olfactory bulb and the CA3 region of the hippocampus reveal a weaker and delayed enhancement of about 10–25% SNR increase, which lasts for up to 48 hr.

Rapidly Enhancing Structures

Figure 2 compares MR images of a mouse brain obtained before (left) and 6 hr after (right) $MnCl_2$ injection. The choroid plexus, pineal gland, and anterior pituitary gland are less well observable without Mn^{2+} contrast, but the posterior lobe of the pituitary gland can be readily identified. After $MnCl_2$ injection, all of these structures show a pronounced and rapid enhancement, with a maximum SNR increase at about 6 hr after injection (see also Fig. 1 and Table 1). Of note, the elevated signal in the choroid plexus, pineal gland, and posterior pituitary gland recovered toward basal values within 1–2 days. In contrast, the anterior lobe of the pituitary gland remained enhanced even after 48 hr.

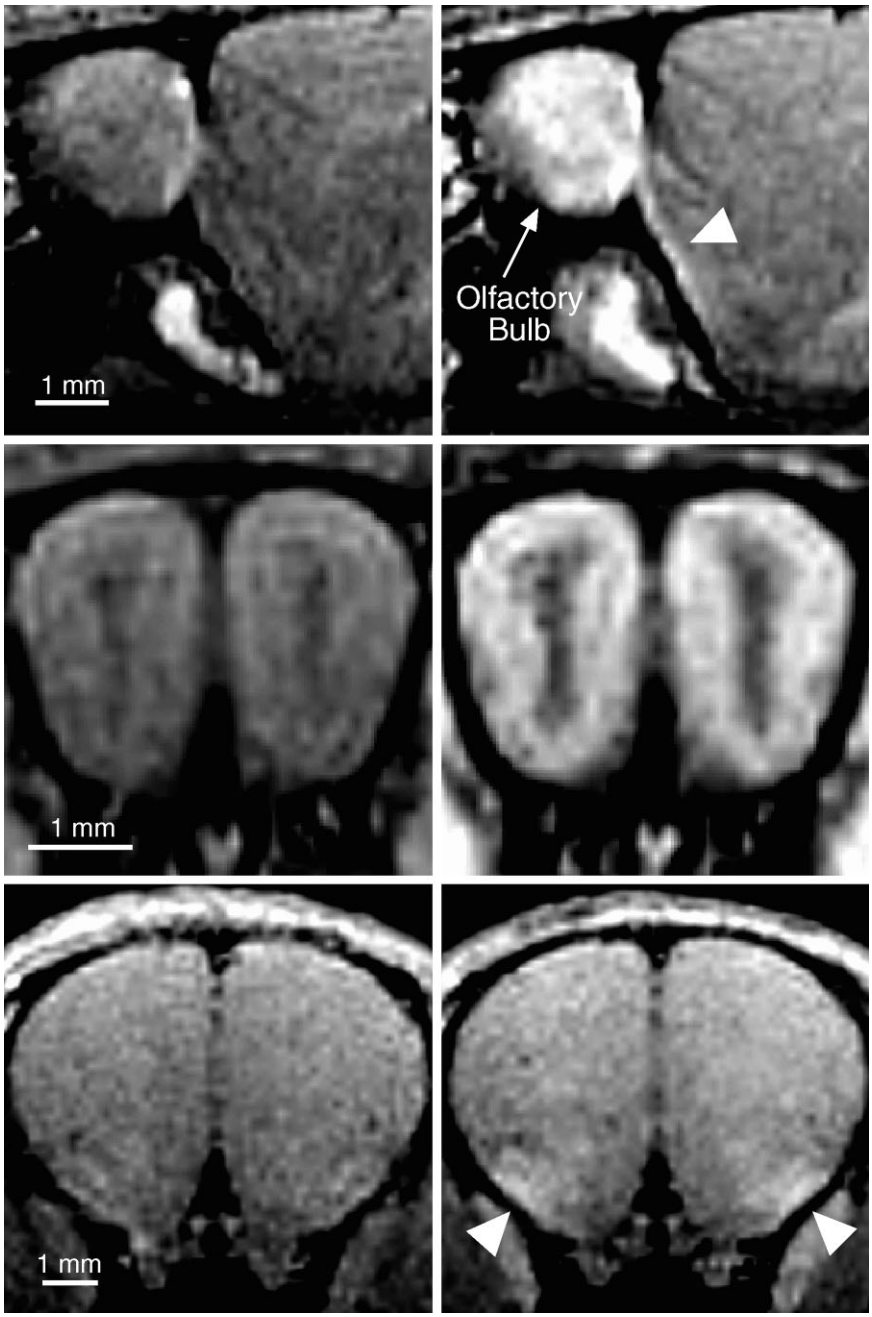

FIG. 3. T_1-weighted MRI of the brain of an anesthetized mouse before (left) and 24 hr after (right) subcutaneous $MnCl_2$ (other parameters as in Fig. 2). Top: Signal enhancement in the olfactory bulb and in a tract-like structure along the base of the anterior forebrain (arrowhead) in a parasagittal section 1.5 mm lateral to the midline. Middle: Mn^{2+}-induced contrast in the olfactory bulb reveals four layers with alternating signal enhancement in a coronal section. Bottom: Tract-like structures along the base of the anterior forebrain in a coronal section.

The observation of a rapid enhancement of the choroid plexus, pineal gland, and pituitary gland is in line with previous autoradiographic observations (8,13,14) using radioactive Mn^{2+} and MRI (17) after $MnCl_2$ (i.p.). This finding may be explained by the direct vascular supply, as the capillaries traversing these regions are known to be freely permeable to plasma solutes. The subsequent decrease of the SNR supports this explanation, because systemically administered Mn^{2+} has been reported to be rapidly cleared from blood and secreted into the bile (21). The prolonged enhancement of the anterior pituitary gland indicates retention and continous accumulation of manganese in this endocrine tissue. It may reflect a special uptake mechanism reported for Ca^{2+} channels of cells of the anterior pituitary (22).

Slowly Enhancing Structures

In addition to tissue, which exhibits a strong Mn^{2+} contrast as early as a few hours after injection, Figs. 3 and 4

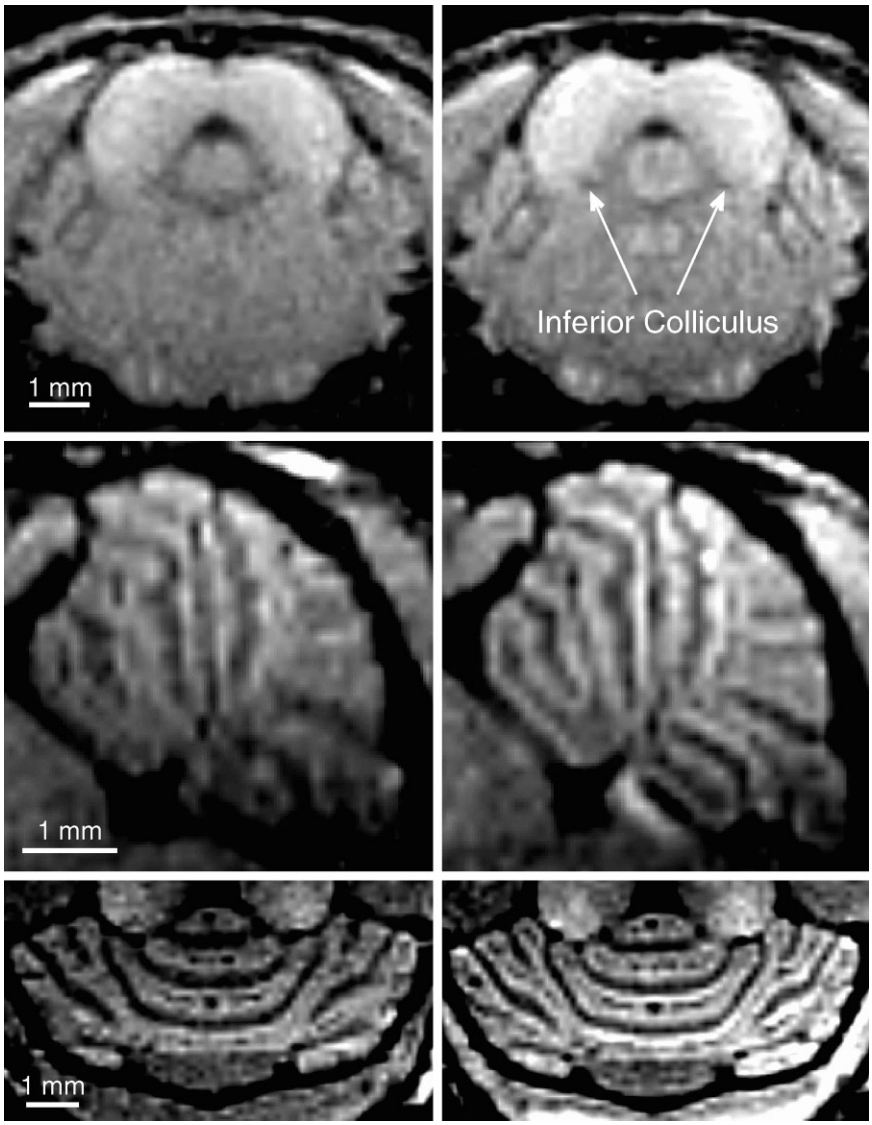

FIG. 4. T_1-weighted MRI of the brain of an anesthetized mouse before (left) and 24 hr after (right) subcutaneous $MnCl_2$ (other parameters as in Fig. 2). Top: Signal enhancement in the inferior colliculi in a coronal section. Mn^{2+}-induced contrast in the cerebellum reveals a laminar structure in a midsagittal (middle) and horizontal (bottom) section.

show T_1-weighted images of enhanced structures at 24 hr after subcutaneous $MnCl_2$. The penetration of the BBB and the distribution of Mn^{2+} in the extracellular space, as well as a subsequent neuronal uptake and axonal transport, may be responsible for the development of correspondingly slower SNR increases. While the former processes could explain the observed tendency for signal increases as seen, for example, in the frontal cortex and basal ganglia (Table 1), the latter mechanisms cause a specific enhancement that, apart from uptake properties, depends on brain function.

Figure 3 demonstrates a marked Mn^{2+}-induced enhancement of the olfactory bulb, which presents as four concentrically arranged layers with alternating high and low signals when passing from superficial to deep layers (Fig. 3, middle right). In comparison with histologic findings (23,24), the high signals probably originate from the glomerular layer and the mitral cell layer with adjacent plexiform layers. In addition, tract-like structures become enhanced bilaterally at the ventral surface of the anterior forebrain (Fig. 3, top and bottom right). Rostrally connected to the olfactory bulb, the elevated signal can be observed about 2.5 mm along the cranial base. In agreement with previous tracing studies (23), this structure most likely represents the lateral olfactory tract, which provides further evidence for the uptake and axoplasmic transport of Mn^{2+} by secondary olfactory neurons. The interpretation is supported by the observation that the deeper of the two bright layers within the olfactory bulb appears to include the mitral cell layer, which consists of comparatively large somata of the principal secondary olfactory neurons.

Figure 4 shows the achievable Mn^{2+} contrast in the inferior colliculi and cerebellum. The inferior colliculi yield relatively high signal intensities in the basal state because of a correspondingly short T_1 relaxation time. Subcutaneous $MnCl_2$ increases the contrast to neighboring tissue even further (Fig. 4, top right). Similarly, $MnCl_2$ injection improves the delineation of layered structures within the cerebellum (Fig. 4, middle right and bottom right). An outer bright layer circumscribes an interior region without a substantial SNR increase after Mn^{2+} appli-

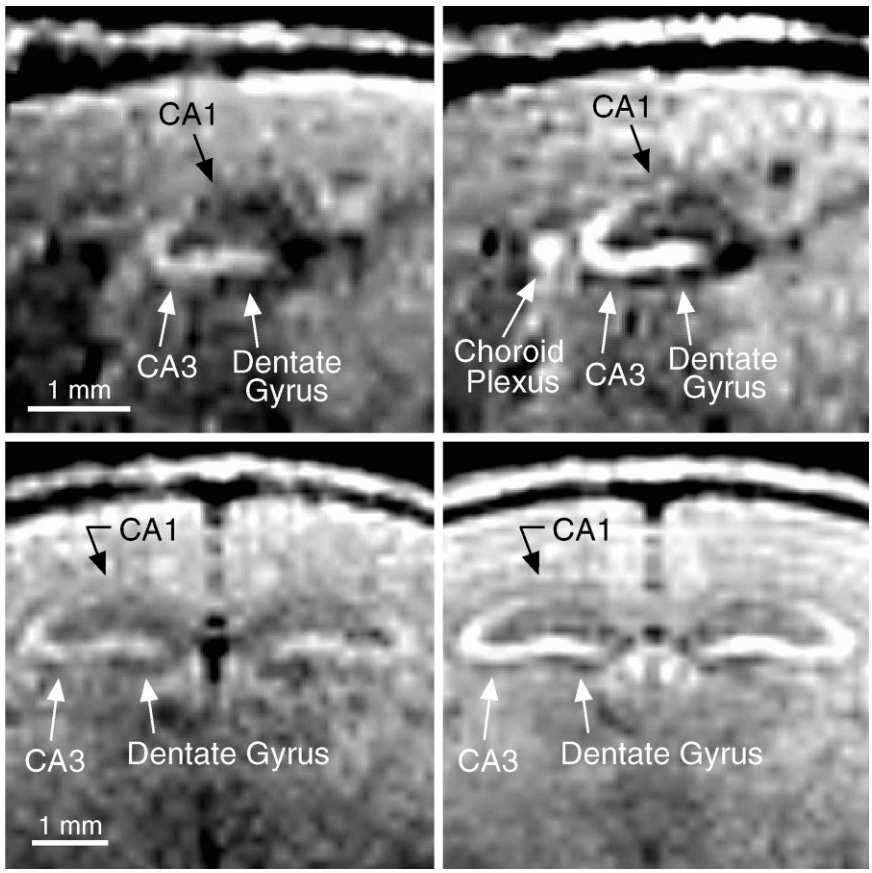

FIG. 5. T_1-weighted MRI of the brain of an anesthetized mouse before (left) and 24 hr after (right) subcutaneous $MnCl_2$ (other parameters as in Fig. 2). Top: Signal enhancement in the CA3 subfield and dentate gyrus of the dorsal hippocampus in a parasagittal section 1.5 mm lateral to the midline. Bottom: Signal enhancement in the dorsal hippocampus in a coronal section.

cation. Based on conventional histology (25,26), the bright signals within the cerebellar cortex probably originate from the Purkinje cell layer and adjacent areas, while the interior non-enhancing areas represent white matter.

Hippocampus

Figure 5 shows the effect of Mn^{2+} on the hippocampal formation. Specific details are readily resolved in sagittal (top) and coronal (bottom) sections due to the high isotropic resolution of the 3D gradient-echo images. A C-shaped structure with relatively high signal intensities in the basal state (top left) extends from the dentate gyrus to the CA3 subfield of the hippocampus. After Mn^{2+} injection, these structures are further enhanced. However, such a signal increase, is not observed within the CA1 subfield. These findings are confirmed in Fig. 6, which compares histologic sections of the mouse brain (27) at two different levels of the hippocampus with corresponding T_1-weighted images before (left) and after (middle) Mn^{2+} administration. Again, high signals in both the middle and ventral sections of the hippocampus are further enhanced after Mn^{2+} injection. Confocal laser scanning microscopy identified the stratum pyramidale (SP), stratum lucidum (SL) (containing the mossy fibers), hilus (H), granule cell layer (GL), and isolated neurons (white dots). In comparison with these histologic data, the microstructures contrasted by Mn^{2+}-enhanced MRI most likely originate from the mossy fibers and adjacent pyramidal cell layer of the CA3 subfield, as well as from the dentate hilus, with parts of the adjacent granule cell layer.

The relatively bright signal in Ammon's horn before Mn^{2+} injection refers to a smaller T_1 relaxation time in the cytoplasm and nucleus than in the extracellular space (28). Typically, a high cellular density or tight packing (as in white matter) leads to a fast T_1 relaxation process. This explanation is in line with morphologic studies of the mouse Ammon's horn (29), which indicate that "the pyramidal layer is thick and manifests three or four rows of cells between which there is no more space than that necessary to contain the intercellular plexus" (page 17). In addition, the mossy fibers are reported to "make up a heavy bundle which travels above the giant pyramids" (page 37) in the CA3 subfield.

Mechanisms

After subcutaneous application of $MnCl_2$ the brain becomes exposed to Mn^{2+} by systemic circulation. Direct access is provided to structures without a BBB, which therefore exhibit both a rapid and pronounced signal enhancement in T_1-weighted MRI. The effect results from a reduction of the T_1 relaxation time of water protons due to neighboring paramagnetic Mn^{2+} ions. In addition to transient accumulation in the choroid plexus and the pituitary and pineal glands, Mn^{2+} ions cross the BBB via the capillary endothelium (13–15) and thus enter the brain and CSF. These unspecific mechanisms most likely contribute

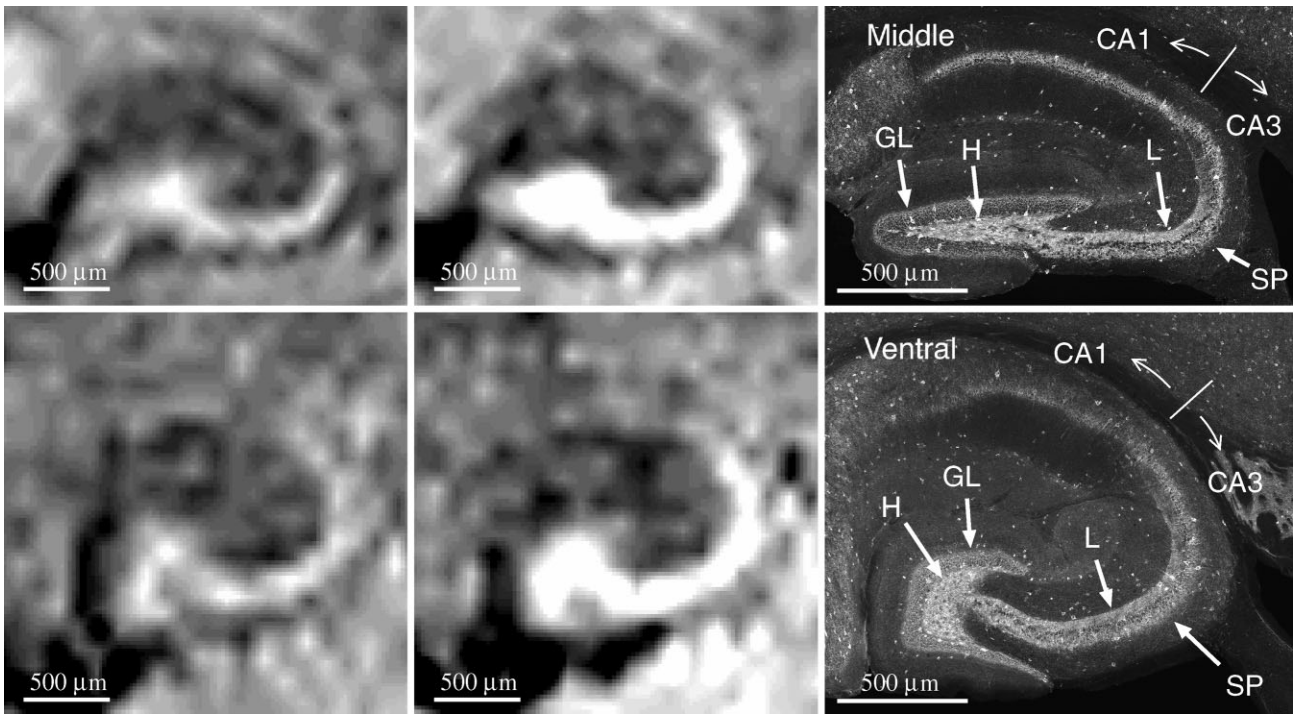

FIG. 6. T_1-weighted MRI of the brain of an anesthetized mouse before (left) and 48 hr after (middle) subcutaneous $MnCl_2$ (other parameters as in Fig. 2) in comparison with histologic sections (right) (courtesy of Jinno et al. (27)) (GL = granule cell layer, H = hilus, L = stratum lucidum, SP = stratum pyramidale). The section orientation is perpendicular to the dorsoventral axis of the hippocampal formation. Top: At the middle level of the hippocampus, the signal enhancement is most pronounced in the stratum pyramidale in CA3, stratum lucidum, and hilus. Bottom: Corresponding findings in the ventral hippocampus.

to the observed tendency for the SNR increase throughout the brain.

The specific MRI enhancement of brain structures by Mn^{2+} is a consequence of its uptake by neurons through Ca^{2+} channels during depolarization (30,31). This phenomenon has been exploited for mapping brain functions by introducing free Mn^{2+} into the rat brain after pharmacologic opening of the BBB (32,33). The procedure causes an activation-induced accumulation of Mn^{2+} in relevant brain systems. Although the present study did not facilitate the Mn^{2+} transfer through the BBB, the distinct signal increases in parts of the olfactory and auditory systems, as well as in the cerebellum and hippocampal formation, are likely to reflect brain activity of the animals integrated over time after $MnCl_2$ administration. Apart from neuronal uptake, part of the observed enhancement requires axoplasmic transport of Mn^{2+} ions. Anterograde transport of radioactive Mn^{2+} after microinjection into the rat basal ganglia has been found to result in a region-specific accumulation and retention for at least 72 hr (34). Recent MRI adaptations utilized axonal Mn^{2+} transport to delineate the olfactory and visual pathway in rodents (20,35). In the present study, the pronounced Mn^{2+} contrast in the lateral olfactory tract and the olfactory bulb strongly suggests an axoplasmic transport by active secondary olfactory neurons. MRI enhancement in other structures, such as the hippocampal mossy fibers, may also be ascribed to this mechanism.

Finally, contributions to the observed MRI signal enhancement may also arise from the distribution of Mn^{2+}-dependent enzymes such as glutamine synthetase and superoxide dismutase (15). Glutamine synthetase is an astrocyte-specific protein that contains eight Mn^{2+} ions and accounts for approximately 80% of the total manganese in brain (36). More specifically, manganese superoxide dismutase was found to be localized in the mitochondria of rat hippocampus (37). In agreement with the present observation of a pronounced Mn^{2+} effect in the Ammon's horn, CA3 pyramidal cells were strongly immunostained by superoxide dismutase, whereas CA1 pyramidal cells were only weakly reactive.

CONCLUSIONS

In summary, the present results demonstrate enhanced soft-tissue contrast in T_1-weighted MRI of murine brain in vivo after subcutaneous administration of $MnCl_2$. Apart from signal increases in structures without a BBB, the specific enhancement of several brain systems suggests the neuronal uptake and axonal transport of Mn^{2+} in response to brain function of behaving animals. Although a more detailed elucidation and assignment of pathways and mechanisms that contribute to the cerebral distribution of Mn^{2+} requires additional studies using conventional histology, Mn^{2+}-based MRI staining techniques have the potential to become a powerful tool for phenotyping mutant mice with an abnormal morphologic and functional organization of the brain.

ACKNOWLEDGMENTS

The authors thank Dr. Shozo Jinno from the Department of Anatomy and Neurobiology, Faculty of Medicine, Kyushu University, for providing the confocal laser microscopic images used in Fig. 6.

REFERENCES

1. Kornguth S, Anderson M, Markley JL, Shedlovsky A. Near-microscopic magnetic resonance imaging of the brains of phenylalanine hydroxylase-deficient mice, normal littermates, and of normal BALB/c mice at 9.4 Tesla. NeuroImage 1994;1:220–229.
2. Munasinghe JP, Gresham GA, Carpenter TA, Hall LD. Magnetic resonance imaging of the normal mouse brain. Lab Anim Sci 1995;45:674–679.
3. Bouilleret V, Nehlig A, Marescaux C, Namer IJ. Magnetic resonance imaging follow-up of progressive hippocampal changes in a mouse model of mesial temporal lope epilepsy. Epilepsia 2000;41:642–650.
4. Kooy FR, Verhoye M, Lemmon V, Van Der Linden A. Brain mouse models for neurogenetic disorders using in vivo magnetic resonance imaging (MRI). Eur J Hum Genet 2001;9:153–159.
5. McDaniel B, Sheng H, Warner DS, Hedlund LW, Benveniste H. Tracking brain volume changes in C57BL/6J and ApoE-deficient mice in a model of neurodegeneration: a 5-week longitudinal micro-MRI study. NeuroImage 2001;14:1244–1255.
6. Natt O, Watanabe T, Boretius S, Michaelis T, Frahm J. In vivo high-resolution MRI of mouse brain at low field (2.35 T). In: Proceedings of The 10th Annual Meeting of ISMRM, Honolulu, 2002; p 1253.
7. Johnson GA, Cofer GP, Gewalt SL, Hedlund LW. Morphologic phenotyping with MR microscopy: the visible mouse. Radiology 2002;222:782–793.
8. Takeda A, Akiyama T, Sawashita J, Okada S. Brain uptake of trace metals, zinc and manganese, in rats. Brain Res 1994;640:341–344.
9. Takeda A, Sawashita J, Okada S. Biological half-lives of zinc and manganese in rat brain. Brain Res 1995;695:53–58.
10. Takeda A, Ishiwatari S, Okada S. In vivo stimulation-induced release of manganese in rat amygdala. Brain Res 1998;811:147–151.
11. Sotogaku N, Oku N, Takeda A. Manganese concentration in mouse brain after intravenous injection. J Neurosci Res 2000;61:350–356.
12. Gallez B, Baudelet C, Geurts M. Regional distribution of manganese found in the brain after injection of a single dose of manganese-based contrast agents. Magn Reson Imaging 1998;16:1211–1215.
13. Murphy VA, Wadhwani KC, Smith QR, Rapoport SI. Saturable transport of manganese(II) across the rat blood-brain barrier. J Neurochem 1991;57:948–954.
14. Rabin O, Hegedus L, Bourre JM, Smith QR. Rapid brain uptake of manganese(II) across the blood-brain barrier. J Neurochem 1993;61:509–517.
15. Aschner M. Manganese homeostasis in the CNS. Environ Res A 1999;80:105–109.
16. Lauterbur PC, Mendonca-Dias MH, Rudin AM. Augmentation of tissue water proton spin-lattice relaxation rates by in vivo addition of paramagnetic ions. In: Dutton PL, Leigh LS, Scarpaa A, editors. Frontier of biological energetics. New York: Academic Press; 1978; p 752–759.
17. London RE, Toney G, Gabel SA, Funk A. Magnetic resonance imaging studies of the brains of anesthetized rats treated with manganese chloride. Brain Res Bull 1989;23:229–235.
18. Newland MC, Ceckler TL, Kordower JH, Weiss B. Visualizing manganese in the primate basal ganglia with magnetic resonance imaging. Exp Neurol 1989;106:251–258.
19. Kim SH, Chang KH, Chi JG, Cheong HK, Kim JY, Kim YM, Han MH. Sequential change of MR signal intensity of the brain after manganese administration in rabbits. Invest Radiol 1999;34:383–393.
20. Watanabe T, Michaelis T, Frahm J. Mapping of retinal projections in the living rat using high-resolution 3D gradient-echo MRI with Mn^{2+}-induced contrast. Magn Reson Med 2001;46:424–429.
21. Bertinchamps AJ, Miller ST, Cotzias GC. Interdependence of routes excreting manganese. Am J Physiol 1966;211:217–224.
22. Ciu ZJ, Dannies PS. Thyrotropin-releasing hormone mediated Mn^{2+} entry in perfused rat anterior pituitary cells. Biochem J 1992;283:507–513.
23. Shipley MT, Adamek GD. The connections of the mouse olfactory bulb: a study using orthograde and retrograde transport of wheat germ agglutinin conjugated to horseradish peroxidase. Brain Res Bull 1984;12:669–688.
24. Royet JP, Souchier C, Jourdan F, Ploye H. Morphometric study of the glomerular population in the mouse olfactory bulb: numerical density and size distribution along the rostrocaudal axis. J Comp Neurol 1988;270:559–568.
25. Ozol K, Hayden JM, Oberdick J, Hawkes R. Transverse zones in the vermis of the mouse cerebellum. J Comp Neurol 1999;412:95–111.
26. Yamada K, Fukaya M, Shibata T, Kurihara H, Tanaka K, Inoue Y, Watanabe M. Dynamic transformation of Bergmann glial fibers proceeds in correlation with dendritic outgrowth and synapse formation of cerebellar Purkinje cells. J Comp Neurol 2000;418:106–120.
27. Jinno S, Aika Y, Fukuda T, Kosaka T. Quantitative analysis of GABAergic neurons in the mouse hippocampus, with optical disector using confocal laser scanning microscope. Brain Res 1998;814:55–70.
28. Schoeniger JS, Aiken N, Hsu E, Blackband SJ. Relaxation-time and diffusion NMR microscopy of single neurons. J Magn Reson B 1994;103:261–273.
29. Ramón y Cajal S. The structure of Ammon's horn. Springfield, IL: Charles C. Thomas; 1968.
30. Drapeau P, Nachshen DA. Manganese fluxes and manganese-dependent neurotransmitter release in presynaptic nerve endings isolated from rat brain. J Physiol 1984;348:493–510.
31. Narita K, Kawasaki F, Kita H. Mn and Mg influxes through Ca channels of motor nerve terminals are prevented by verapamil in frogs. Brain Res 1990;510:289–295.
32. Lin YJ, Koretsky AP. Manganese ion enhances T_1-weighted MRI during brain activation: an approach to direct imaging of brain function. Magn Reson Med 1997;38:378–388.
33. Duong TQ, Silva AC, Lee AP, Kim SG. Functional MRI of calcium-dependent synaptic activity: cross correlation with CBF and BOLD measurements. Magn Reson Med 2000;43:383–392.
34. Sloot WN, Gramsbergen JP. Axonal transport of manganese and its relevance to selective neurotoxicity in the rat basal ganglia. Brain Res 1994;657:124–132.
35. Pautler RG, Silva AC, Koretsky AP. In vivo neuronal tract tracing using manganese-enhanced magnetic resonance imaging. Magn Reson Med 1998;40:740–748.
36. Wedler FC, Denman RB. Glutamine synthetase: the major Mn (II) enzyme in mammalian brain. Curr Top Cell Regul 1984;24:153–169.
37. Akai F, Maeda M, Suzuki K, Inagaki S, Takagi H, Taniguchi N. Immunocytochemical localization of manganese superoxide dismutase (Mn-SOD) in the hippocampus of the rat. Neurosci Lett 1990;115:19–23.